Journal of Membrane Science 700 (2024) 122726

Contents lists available at ScienceDirect

Journal of Membrane Science

journal homepage: www.elsevier.com/locate/memsci

Gamma-irradiated janus electrospun nanofiber membranes for desalination and nuclear wastewater treatment

Mohamed Essalhi [a,b], Noor Ul Afsar [a], Denis Bouyer [c], Ola Sundman [a], Michael Holmboe [a], Mohamed Khayet [d], Mats Jonsson [e], Naser Tavajohi [a,*]

[a] Department of Chemistry, Umeå University, 90187, Umeå, Sweden
[b] African Sustainable Agriculture Research Institute (ASARI), Mohammed VI Polytechnic University (UM6P), Laâyoune, 70000, Morocco
[c] Institut Européen des Membranes, IEM, UMR 5635, ENSCM, CNRS, Univ Montpellier, Montpellier, France
[d] Department of Structure of Matter, Thermal Physics and Electronics, Faculty of Physics, University Complutense of Madrid, Avda. Complutense s/n, 28040, Madrid, Spain
[e] Department of Chemistry, KTH Royal Institute of Technology, SE - 100 44, Stockholm, Sweden

ARTICLE INFO

Keywords:
Double-layer electrospun nanofibrous membranes
Hydrophobic/hydrophilic
Desalination
Membrane distillation
Simulated nuclear wastewater treatment
Nuclides decontamination

ABSTRACT

This study presents the fabrication of double-layer electrospun nanofibrous membranes (DL-ENMs) using polyvinylidene fluoride (PVDF) and polyether sulfone (PES) based polymers with different degrees of hydrophilicity (PES, sulfonated PES, and PES with hydroxyl terminals). A comparative analysis was carried out with single-layer electrospun nanofiber membranes (SL-ENM) with a total thickness of about 375 μm. Using feed solutions, including sodium chloride, sodium nitrate, and simulated nuclear wastewater (SNWW), the performance of DL-ENMs was evaluated for desalination and radionuclide decontamination by direct contact membrane distillation (DCMD) and air gap membrane distillation (AGMD) techniques. The results showed that DL-ENMs, especially those incorporating a sulfonated PES-based hydrophilic layer, exhibited superior permeate fluxes, reaching values of 72.72 $kg/m^{2}\cdot h$ and 73.27 $kg/m^{2}\cdot h$ in the DCMD using aqueous feed solutions of NaCl and $NaNO_3$, respectively, and 70.80 $kg/m^{2}\cdot h$ and 41.96 $kg/m^{2}\cdot h$ using aqueous feed solutions of SNWW in DCMD and AGMD, respectively. Both SL-ENMs and DL-ENMs exhibited high rejection efficiencies and decontamination factors for the feed solutions (>99.9%). In addition, the prepared ENMs were exposed to gamma radiation to evaluate their applicability in real-life applications. The result of irradiation revealed the negative impact of gamma radiation on the fluorine content of PVDF which could be a critical point in using PVDF as a hydrophobic material for decontaminating nuclear wastewater by membrane distillation.

1. Introduction

Radioactive liquid wastes are generated from a variety of sources [1]. These include nuclear power reactors, radioisotope production facilities, uranium enrichment facilities, institutional research centers that produce radiopharmaceuticals, and laundries at nuclear facilities [2]. These facilities must properly manage and dispose of the significant amount of hazardous waste they generate [2]. To minimize the risk of contamination and protect public safety, it is critical to implement effective measures to ensure the safe handling and disposal of radioactive liquid waste [3–5].

Interest in radioactive wastewater treatment has increased substantially in the aftermath of the catastrophic accident at the Fukushima nuclear power plant (Japan, March 11, 2011) and because of a desire to support the sustainable development of the nuclear power industry [6]. According to data reported by Japan, 64 radionuclides, including Cs-137, Co-60, and Cr-51, exist in nuclear wastewater that can persist for long periods in the environment since their half-lives range from a few years to several centuries [6,7]. These radionuclides have the potential to bioaccumulate in aquatic organisms, primarily in fish and crustaceans, and subsequently reach the food chain, resulting ultimately in adverse human health consequences such as radiation poisoning and heightened cancer risk [8]. In addition, the effects of releasing nuclear wastewater into the ocean are not limited to the immediate site of the release. Ocean currents and circulation patterns allow contaminated water to be transported long distances, affecting marine ecosystems and

---

[*] Corresponding author.
E-mail address: naser.tavajohi@umu.se (N. Tavajohi).

https://doi.org/10.1016/j.memsci.2024.122726
Received 1 January 2024; Received in revised form 25 March 2024; Accepted 31 March 2024

human populations far from the source [9]. This underscores the need to take a comprehensive approach to dealing with nuclear effluents, considering the potential long-term effects on both the environment and human health.

For the treatment of radioactive wastewater, several techniques have been developed. These include evaporative processes, chemical precipitators, conventional filtration, ion exchange, biological treatment, and membrane distillation-based processes [3,10–16]. It is important to carefully consider which approach is best for a given situation, as each of these methods has its unique advantages and disadvantages [17,18]. By utilizing these advanced techniques, we can effectively manage and mitigate the risks associated with radioactive wastewater [19–22]. In doing so, we can ensure a safer and more sustainable future for all.

Membrane-based processes are a highly effective method of treating liquid radioactive waste. High decontamination factors, low energy requirements, ease of operation, and the possibility of closed-loop operation are just some of the advantages of these processes. It is important to note, however, that there are several limitations associated with pressure-operated membrane processes [23]. For instance, the separation efficiency falls short of the necessary value (≈100% rejection) for effective nuclear wastewater decontamination. Despite this limitation, the advantages of membrane processes make them an attractive option for the treatment of liquid radioactive waste [23–25]. Furthermore, the separation of the smallest ionic radioisotopes from radioactive waste requires the integration of the pressure membrane process with subsequent chemical post-processing. This leads to the formation of complicated complex-forming compounds that require post-processing [26,27]. Therefore, these complexing compounds need additional filtration following appropriate pH adjustment [27,28]. To address several of the above limitations, non-isothermal membrane distillation (MD) techniques represent a promising alternative.

MD is a thermally driven separation process that could potentially be operated in part using waste/low-grade heat from industrial facilities plants, especially in the nuclear industry, where removing radioactive contaminants is paramount. Furthermore, with the use of waste heat or low-grade heat, the MD processes can substantially reduce their energy consumption and operating costs.

This technology uses a hydrophobic microporous membrane to separate feed from permeate, at different temperatures [29]. The membrane prevents liquid mass transfer by creating a vapor-liquid interface and allowing water vapor to pass through and condense, resulting in purified water [29]. A vapor pressure difference is the driving force behind the transport of water molecules across the membrane, resulting in a theoretical rejection efficiency of 100% for solutes of concern, for example, radionuclides [30]. Four types of MD processes exist, differing in terms of the configuration of the distillation system on the permeate side of the membrane [31]: direct contact membrane distillation (DCMD), vacuum membrane distillation (VMD), air-gap membrane distillation (AGMD), and swept gas membrane distillation (SGMD) [32]. The most intensively studied configuration is DCMD [30].

The membrane material's properties and geometry greatly influence MD's effectiveness. Notably, most commercially available membranes used in MD were designed originally for microfiltration processes and not specifically for MD. Therefore, growing interest is in developing new membranes specifically tailored for MD. These new membranes should preferably exhibit high levels of hydrophobicity and stability over a wide range of operating conditions. They should also have narrow pore size distributions and favorable structural and morphological properties. By developing such membranes, we will be able to improve the efficiency and effectiveness of MD processes significantly.

MD application membranes can be manufactured in different configurations, such as flat sheets, hollow fibers, or electrospun nanofibrous membranes (ENMs). The ENMs may possess different geometrical structures such as single-, dual- and triple-layered structures [33,34]. Recently, electrospinning technology for fabricating ENMs received a significant boost due to the exceptional accomplishments of prepared membranes in the desalination and wastewater treatment fields [35–37]. Additionally, ENMs have several advantages over other MD membranes, including greater hydrophobicity, higher void volume fraction with an interconnected pore structure, customizable pore size, and controllable thickness [38]. These features make ENMs interesting candidates for the decontamination of nuclear waste using the MD method.

Numerous methods have been proposed to improve the efficiency and properties of MD. Dual-layer hydrophobic/hydrophilic membranes (DL-ENMs), which have been shown to outperform hydrophobic monolayer membranes (SL-ENMs) of the same thickness, are a particularly noteworthy approach [39,40]. These membranes are composed of a thin, porous hydrophobic layer and a thicker, supportive hydrophilic layer with larger pores that provide mechanical strength and reduce conduction heat loss and mass transfer resistance between the evaporating side and the condensing side [41]. Importantly, MD performance is highly sensitive to the properties of both layers.

Prior research suggests that combining a thinner hydrophobic layer with a thicker hydrophilic layer can improve flux. However, the influence of the support layer's hydrophilicity on MD performance has yet to be determined. As such, this study aims to explore the impact of the support layer's hydrophilicity on the flux performance of DL-ENMs. Furthermore, this study examines the impacts of absorbed dose gamma irradiation (<100 kGy) emitted from a cesium source (Cs-137) on the physicochemical properties of the engineered ENMs and studies their stability during desalination and decontamination of SNWW contaminated with three types of nuclides (cesium, cobalt, and chromium) using DCMD and AGMD. In addition, commercial nanofiltration membranes were also evaluated for permeate flux and radionuclide selectivity and compared with the DL-ENM evaluated in MD. The results of this study shed light on the effect of gamma irradiation on the stability and performance of PVDF as a dominant fluoropolymer in MD applications.

2. Experimental

2.1. Materials

Polyethersulfone (PES; 5200P, $M_W = 45000$ g mol^{-1}), hydroxyl-terminated polyethersulfone (PES-OH) possesses an OH abundance of 70% (5003 PS, $M_W = 45000$ g mol^{-1}), sulfonated polyethersulfone (PESS) with a sulfonation degree (SD) of 30% ($M_W = 119000$ g mol^{-1}), and polyvinylidene fluoride (PVDF) (Solef 1015, MW = 275000 g mol^{-1}) were kindly supplied by Sumitomo chemical company and Solvay Specialty Polymers. Kerosene (used as a wetting agent for void volume fraction measurement), Acetone, $Co(NO_3)_2{\cdot}6H_2O$ (>98%), $CrCl_3^{\cdot}6H_2O$ (96%), CsCl (>98%), NaCl (99%), and $NaNO_3$ (>99%) were purchased from Sigma–Aldrich Chemical Co. CPI International provided 1000 ppm stock solutions of cesium (Cs), cobalt (Co), and chromium (Cr) in 2.5% HNO_3 for creating calibration standards. All chemicals were used without further purification. Commercial Nanofiltration membranes ESNA1LF, and NANO-SW were kindly provided by Nitto Denko Corporation. TriSep™ TS80, TriSep™ TS40, Microdyn NP010, and Microdyn NP030 were purchased from Microdyn-Nadir.

2.2. Membrane preparation

Homogeneous polymer solutions were prepared by dissolving 25 wt % of PVDF, 32.5 wt% of PES, 32.5 wt% of PES-OH, or 27.5 wt% of PESS with a combined solvent of acetone and DMAC (20/80 wt%) at 50 °C while stirring at 120 rpm. The polymer solutions were degassed overnight at room temperature before the electrospinning process. The ionic conductivity (χ) and viscosity (η) of the dope solutions were measured using a conductivity monitor (edge, model HI2003, Hanna Instruments Inc., USA) and a digital Viscometer (METTLER RM180 Rheomat, Mettler-Toledo AG) as listed in Table 1. All measurements were

Table 1

Electrical conductivity (χ) and viscosity (μ) of the dope solutions (polymer/acetone/DMAC) used to prepare the ENMs.

Polymer structure	χ (μS/cm)	μ (Pa·s)
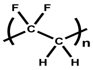	10.46 ± 0.13	3.62 ± 0.19
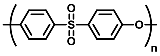	3.65 ± 0.8	3.03 ± 0.27
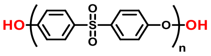	4.43 ± 0.54	2.87 ± 0.13
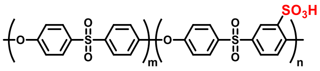	5.35 ± 0.23	3.11 ± 0.04

(*) Hydroxyl-terminated PES (terminal OH groups, abundance $\leqq$70%); Sulfonated PES (Sulfonate groups, sulfonation degree $\leqq$ 30%).

performed at 25.0 ± 0.5 °C.

The DL-ENMs were prepared using a laboratory electrospinning setup with an electrospinning duration of 45 min for each polymer solution. Briefly, the polymer solution was transferred into a 50 mL glass syringe (Nikepal) fitted with a metal needle (inner/outer diameter: 0.6/0.9 mm) and connected to a circulating pump (IPS14-RS, Inovenso). A high-voltage power supply (Genvolt 7xx30 series) was used to provide a positive DC voltage of 25 kV to the needle tip, creating a stable electrified jet flow. Nanofibers were subsequently collected on aluminum foil supported by a circular copper holder with the polymer solutions flowing at 1.25 mL/h, and a 20-cm air gap between the needle tip and the metallic collector. Solvents evaporate as the polymer fiber elongates, whips, stretches, and finally forms a nonwoven matrix on the grounded metal collector during electrospinning. The temperature and humidity were maintained at 25 °C, and 38%, respectively.

Due to the high electrical conductivity of the PVDF solution compared to the PES, PES-OH, and PESS solutions (see Table 1), the electrical charge dissipation towards the collector would be more favorable, resulting in a fibrous network more compacted. ; consequently, the PVDF layer was deposited on the collector first. Conversely, if the PES, PES-OH, or PESS layer was deposited before the PVDF layer, it acts as an insulator, resulting in a less compact web. A SL-ENM was also prepared from the PVDF polymer solution by electrospinning for 1.5 h for comparative purposes. The total electrospinning time of each ENM was 1.5 h. Thus, all DL- and SL-ENMs were roughly the same thickness. Following electrospinning, the ENMs were subjected to post-treatment, which consisted of heating them in an oven at 120 °C for 0.5 h.

2.3. Gamma irradiation

A Cs-137 γ-source was used for the irradiation with a dose of approx. 0.1 Gy/s as previously determined by Fricke dosimetry. The membranes were placed within 20 mL glass vials filled with deionized water and subjected to irradiation for a period of one week, a total dose of approximately 60 kGy.

2.4. Characterization

Field emission scanning electron microscope (FESEM, Carl Zeiss) was used to examine the morphology of the fabricated ENMs. The samples were frozen in liquid N_2, fixed on the sample holder with carbon adhesive tape, and coated with a thin layer of gold using a rotary-pumped sputter coater (QUORUM Q150R S) for 60 s at 20 mA. Using UTHSCSA ImageTool 3.0, SEM images of the ENM surfaces were analyzed to determine their nanofiber diameters (d_f). The mean fibers diameter and standard deviations were obtained for each sample by evaluating the diameters of 100 individual nanofibers and analyzing at least three different images at the same magnification.

Energy-dispersive X-ray spectroscopy (EDX) (X-Max, OXFORD Instruments) was used to investigate the presence or absence of Co, Cr, and Cs on the surface of the ENM samples following their extraction from the MD module. The EDX elemental mapping was performed to scan an area of approximately 500 μm × 500 μm across the surface of the ENM samples. The atomic percentages of Cr, Co, Cs, F, and C, were calculated for each ENMs. Additionally, the ratio of atomic percentages of each element to the sum of fluorine (F) and carbon (F + C) was also determined for each ENM.

Fourier Transform Infrared (FTIR) spectra of ENMs were acquired using a Bruker Vertex 80 spectrometer in the 400-4000 cm^{-1} range with 2 cm^{-1} resolution in attenuated total reflection (ATR) transmission mode.

The surface analysis of both irradiated and unirradiated ENMs were conducted using X-ray photoelectron spectroscopy (XPS, Thermo Scientific K-Alpha, CAE: Pass energy 150.0 eV, Lens Mode: Standard). For this analysis, Mg Kα X-ray radiation (with a power of 72 W, an excitation voltage of 12 kV, and an energy resolution of 1 eV) was employed as the excitation source. A multi-channel hemispherical electron analyzer was used to record high-resolution spectra of C-1s, O-1s, and F-1s in the binding energy range of 0–1200 eV. The measurements were taken at a take-off angle of 58°, corresponding to 8 nm from the sample's hydrophobic surface (i.e., PVDF layer).

To determine the void volume fraction (ε), the dry weight (w_{td}) and wet weight (w_{tw}) of the membranes were measured before and after immersing in kerosene for 24 h. The difference between the dry and wet weights was then used to calculate the volume of the inter-fiber space. The void volume fraction was calculated using the following equation:

$$\varepsilon\,(\%) = \frac{\frac{w_{tw}-w_{td}}{\rho_k}}{\frac{w_{tw}-w_{td}}{\rho_k}+\frac{w_{td}}{\rho_p}} \times 100 \tag{1}$$

where ρ_k is the density of kerosene and ρ_p is the density of the polymer at room temperature. Three measurements were performed for each ENM using samples with a surface area of approximately 2 cm × 1 cm.

Inter-fiber space (d_i) was determined using a gas-liquid displacement capillary flow porometer (CFP; POROLUXTM 100, IB-FT Germany) in conjunction with a liquid wetting agent (POROFIL125). Initially, ENM samples with diameters of 18.5 mm were wetted with POROFIL125 and placed on the porometer's SH 25 sample holder. The sample was then subjected to a stepwise pressure increase at a rate of 80 s/bar, while the gas permeation flux was measured as a function of transmembrane pressure, a characteristic S-shaped “wet curve” was generated. Briefly, during this stage, the flow rate initially remains close to zero with increasing pressure until reaching the bubble point, where the largest inter-fiber space (d_i) becomes empty, and the flow rate continues increasing. Consequently, the inter-fiber spaces de-wetted progressively with increasing pressure, leading to a faster increase in flow rate with pressure until completely de-wetting (i.e., “dry “) of the sample occurs at the point where the trend of increasing flow rate with pressure turns linear and shallow finishing by determining the gas flow-pressure relationship for the dry membrane. Ultimately, from the intersection point of the wet and semi-dry curves (i.e., obtained by having the flow rates measured for the dry membrane), the mean inter-fiber space (d_i) together with the differential filter flux or inter-fiber space distribution (DFF), corresponding to the flux increase per unit increase of the inter-fiber space, could be determined. Each ENM was subjected to at least three experiments with three different samples to determine the inter-fiber space.

A digital micrometer with an accuracy of 0.1 m was used to measure the thickness (δ) of the membrane. The average thicknesses and standard deviations based on measurements performed at ten different locations on each membrane are provided.

Liquid entry pressure (*LEP*) stands as a critical parameter in MD applications, representing the minimum transmembrane pressure required for water to the membrane's largest pores. The measurement of *LEP* was performed in a 47 mm Stirred Cell (Millipore) using DI water and a 35 g/L NaCl aqueous solution. The effective membrane area in this system was 0.00173 m^2. A 25 mL liquid sample was filled into the cell and then subjected to a constant pressure of about 4 kPa using N_2 cylinder flow for 5 min at room temperature. Subsequently, a 2 kPa increase in applied pressure was applied every 2 min, and the applied pressure was recorded as *LEP* when the penetrating liquid became visible in the inter-fiber space at the bottom of the membrane cell. For each type of ENM, the averages of *LEP* and their corresponding standard deviation values represent three different samples.

The water contact angle (θ_w), on both the top and bottom surfaces of each ENM was measured at room temperature employing a computerized optical system (CAM200). It was connected to a CCD camera, an image capture device, and image analysis software. We used a micro-syringe to deposit approximately 10.0 μL droplets of DI water onto the

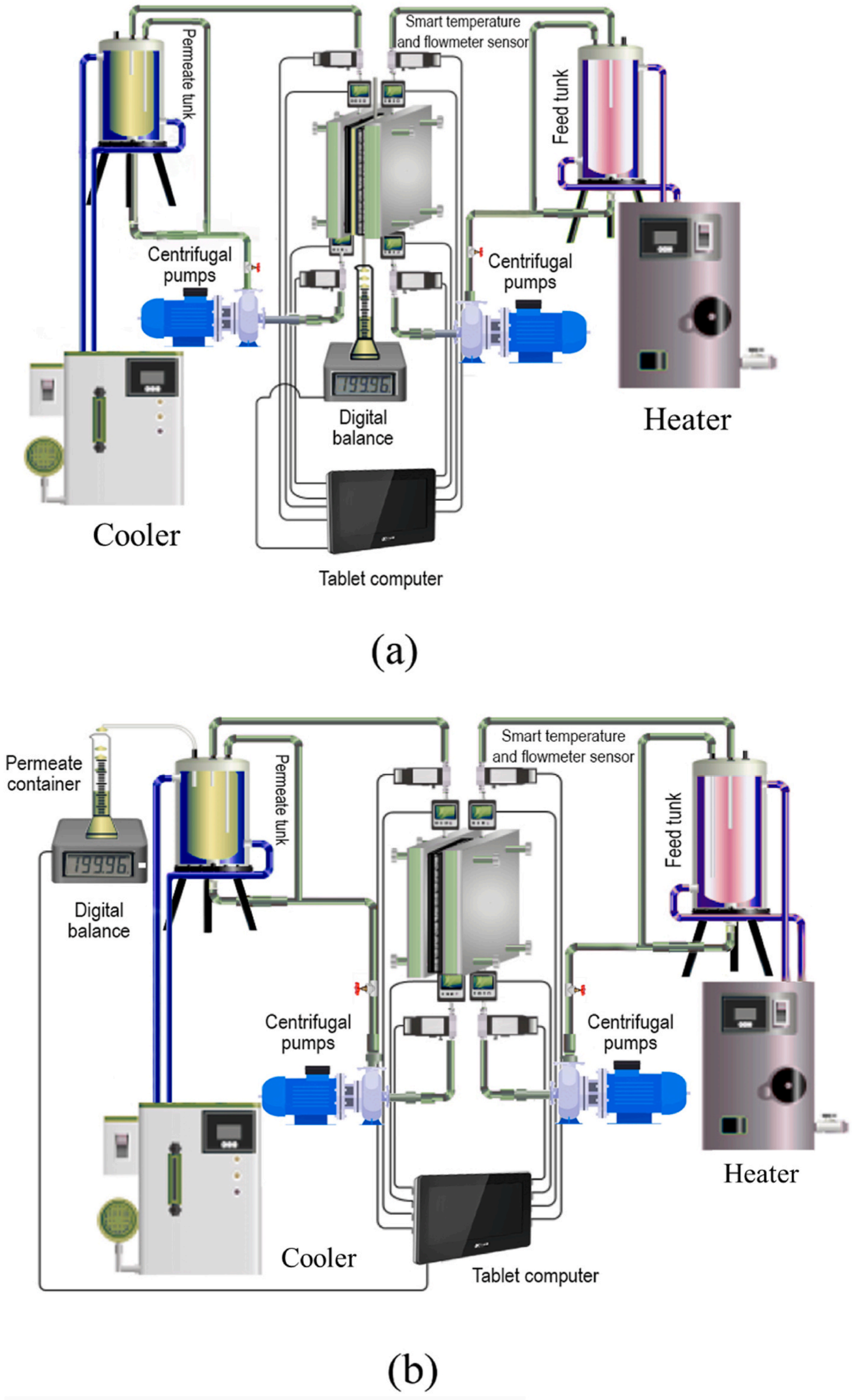

Fig. 1. Schematic design of the a) Air Gap Membrane Distillation and b) Direct Contact Membrane Distillation setup. The inlet temperatures for both permeate ($T_{p,\mathrm{in}}$) and feed ($T_{f,\mathrm{in}}$) were fixed at 20 °C and 70 °C, respectively.

surface of the samples. The images were captured using the Cam200usb software, which automatically performs the left and right side contact angles of each droplet, and the average value was obtained for each sample based on more than 5 measurements.

2.5. *Membrane distillation (MD)*

Direct contact membrane distillation (DCMD) and air gap membrane distillation (AGMD) were used for the separation experiments (see Fig. 1). In the DCMD system, two aqueous solutions at different temperatures circulated simultaneously in direct contact with the ENM through separate channels. Meanwhile, in the AGMD system, one of the two aqueous solutions circulates in direct contact with the ENM, whereas the second aqueous solution (i.e., permeate side) circulates in contact with the metal plate, which determines the air gap. A switchable membrane module (model CPR920, Convergence Industry B·V; The Netherlands) was used with an effective membrane surface area of 0.006 m^2 (0.04 m wide and 0.15 m long). This module was integrated with two flowmeters and four TMU thermometers (Papouch store s.r.o.; Czech Republic) attached *via* USB interfaces to a computer. An electromagnetic thermostat (model EMX5000/SCE, Electrothermal; UK) was employed to control the feed temperature, while a recirculation cooler (model CFT-75, VESLAB instruments. Int.; USA) was utilized to control the permeate temperature. Both inlet and outlet temperatures were automatically recorded at 30-s intervals. Flasks containing the aqueous feed and distillate solutions of a volume of ($V = 1$ m^3) were used. The feed aqueous solution composed of either salty simulated nuclear wastewater or NaCl or $NaNO_3$ solution flowed through the active (hydrophobic) layer. In DCMD, the distilled water circulates over the nanofibrous (hydrophilic) support layer side of the DL-ENM, while for AGMD it passes over the metal plate side.

The simulated nuclear wastewater (SNWW) included CsCl, $CrCl_3{\cdot}6H_2O$, $Co(NO_3)_2{\cdot}6H_2O$, and $NaNO_3$. The simulated aqueous solution contained approximately 450 ppm of each component Cs^+, Cr^{3+}, and Co^{2+} supplemented with 35 g/L $NaNO_3$. $NaNO_3$ was chosen because it is typically present in naturally radioactive wastewater [4,42].

Firstly, DCMD was performed for 3 h using DI water both as feed and permeate aqueous solution to examine potential leakage or damage within the DL-ENMs or the membrane module. Then a desalination experiment using DCMD for 3 h employing 35 g/L NaCl aqueous solution both as a feed and DI water as a permeate, then another 3 h using 35 g/L $NaNO_3$ aqueous solution as a feed and DI water as a permeate. Finally, decontamination experiments were performed using DCMD (6 h) and AGMD (4 h) with SNWW. In the experiments conducted for ENMs, the operating conditions remained unchanged. The total operating time for the MD experiments for each ENM was at least 28 h. The inlet temperatures for both permeate ($T_{p,\mathrm{in}}$) and feed ($T_{f,\mathrm{in}}$) were fixed at 20 °C and 70 °C, respectively, while feed and permeate flow rates were maintained at ~1.25 and 0.75 L min^{-1}, respectively. To identify any possible fouling and/or membrane efficiency changes the permeate flux was measured after each desalination experiment, utilizing DI water as feed and permeate under the same conditions.

The concentrations of Cs^+, Cr^{3+}, and Co^{2+} ions in both the aqueous feed and permeate solutions were determined by employing the inductively coupled plasma optical emission spectrometer (ICP-OES, PerkinElmer, Uberlingen, Germany) equipped with a cross-flow nebulizer and performing elemental analysis using a double nebulizer chamber.

Both salt rejection factor (α) and decontamination factor (DF) were used to determine the desalination and decontamination efficiency by DCMD and AGMD for aqueous salt solutions and SNWW.

The following equation defines the salt rejection factor [9]:

$$\alpha(\%) = \left(1 - \frac{C_p}{C_f}\right) \times 100 \tag{2}$$

where C_f (g/L) and C_p (g/L) represent feed and permeate salt concentrations, respectively.

The DI water in the permeate tank induces the dilution effect in DCMD mode; therefore, to avoid this, the calculation of the salt rejection factor (α) was carried out by correcting the concentration of the permeate produced by the following equation [43,44]:

$$C_p = \frac{C_1 m_1 - C_0 m_0}{m_1 - m_0} \tag{3}$$

where C_0 and C_1 are the initial and final permeate salt concentrations at the permeate tank, and m_0 and m_1 are the initial and final weights of the permeate solution at the tank, respectively.

The following expression defines the decontamination factor:

$$DF = \frac{C_{f,i}}{C_{p,i}} \tag{4}$$

whereas $C_{f,i}$ (ppm) and $C_{p,\mathrm{i}}$ (ppm) represent the nuclide concentration in the feed and permeate water. The *i*-index is related to the ion under consideration, such as Cr^{3+}, Co^{2+}, and Cs^+.

2.6. *Filtration experiment*

The filtration experiments were performed using a Sterlitech HP4750 dead-end filtration cell connected to a N_2 pressurization system at 25 °C and a stirring speed of 250 rpm. The filtration cell had an effective membrane area of 14.6 cm^2 and a volume capacity of 300 mL. The water flux was monitored and recorded using an analytical balance until a stable permeate flux was obtained. Following that, the SNWW was added as feed to the reservoir and filtered through the membrane at a constant pressure of 9 bar. Samples of final filtrate and feed water were collected during each experiment to determine nuclide concentration. Equation (5) was used to calculate the rejection factor β (%).

$$\beta\left(\%\right) = \left(1 - \frac{C_{p,i}}{C_{f,i}}\right) \times 100 \tag{5}$$

whereas $C_{f,i}$ (ppm) and $C_{p,\mathrm{i}}$ (ppm) represent the nuclide concentration in the feed and permeate water. The *i*-index is related to the ion under consideration, such as Cr^{3+}, Co^{2+}, and Cs^+.

3. Results and discussions

3.1. *Morphological characteristics of the prepared DL-ENMs before gamma-irradiation*

SEM and EDS analysis were used to analyze the cross-section and surface composition of both the SL-ENMs and DL-ENMs, as in Fig. 2a. In addition, the mean fiber diameters (d_f) were recorded from the SEM images of the hydrophobic PVDF, and hydrophilic PES, PES-OH, and PESS layers (see Fig. 2). Figure 2d-e shows their corresponding statistical distribution. Furthermore, Fig. 2f shows the EDS surface mapping of PESS DL-ENM highlighting fluorine (in red) linked with PVDF and sulfur (in green) associated with PESS. It can be observed that the fluorine concentration associated with PVDF decreases immediately after the disappearance of the hydrophobic layer of the DL-ENM, while the sulfur and oxygen concentrations associated with PES, PES-OH, and PESS increase. This confirms that a DL-ENM comprises two layers, one hydrophobic and one hydrophilic. It is worth mentioning that a continuous concentration profile along the entire cross-section of the ENM was observed in the case of PVDF SL-ENM as evidenced by the fluorine EDS spectra. Based on the EDS spectra, the hydrophobic layer thickness was 184.6 ± 11 μm. This was expected considering that the total electrospinning time of each ENM was 1.5 h, so the electrospinning time of each layer was 45 min.

The surface morphology of the PVDF layers of the DL-ENMs is characterized by an entangled network of fine nanofibers with multiple

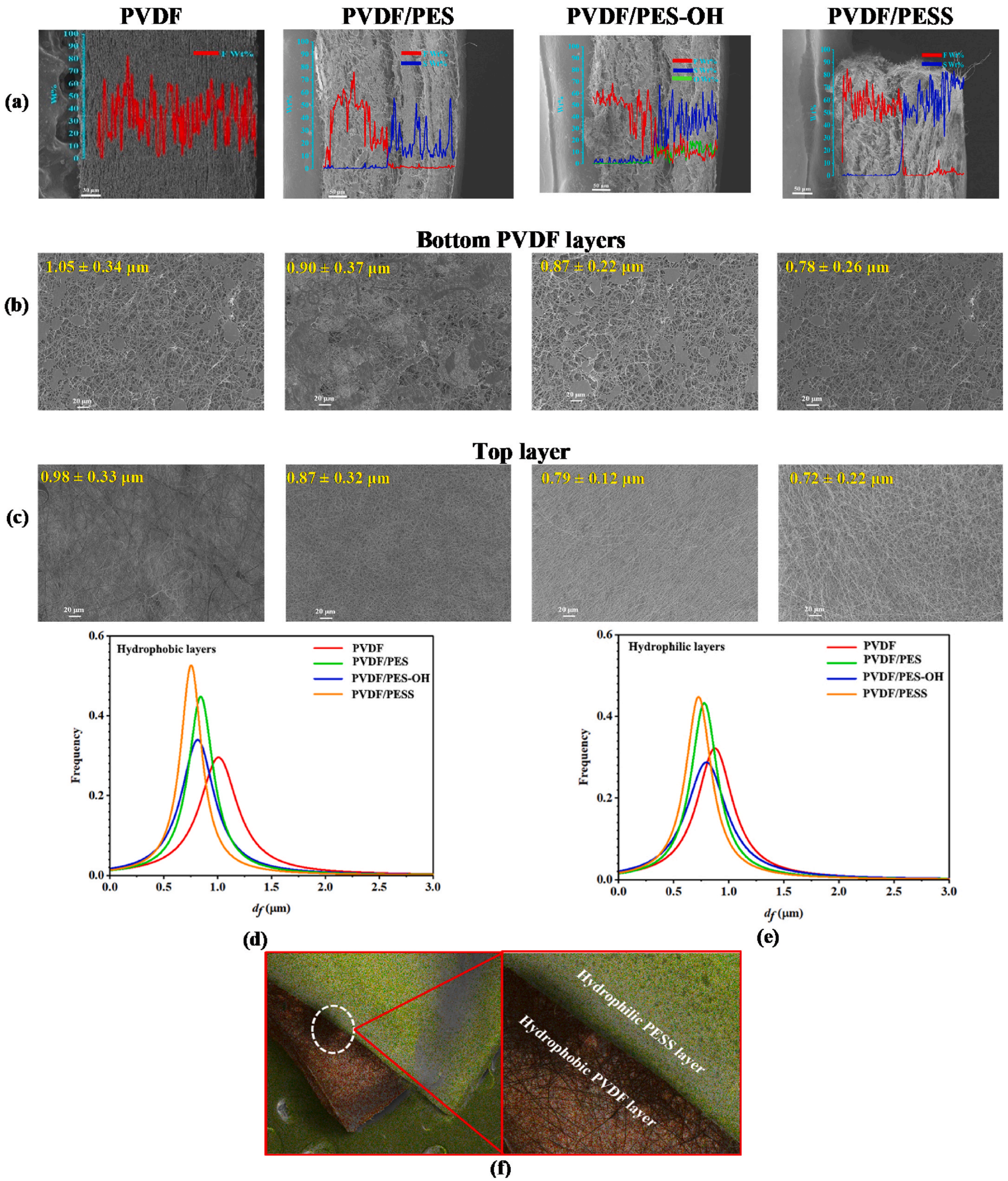

Fig. 2. SEM images and EDS analysis of cross sections of a) prepared SL- and DL-ENM; and SEM images of b) PVDF bottom hydrophobic; c) PES, PES-OH, and PESS top hydrophilic layers, respectively; d) the statistical distribution and mean fiber diameter (d_f) of hydrophobic layer; e) the statistical distribution and d_f of hydrophilic layer; and f) EDS surface mapping of PESS DL-ENM of F (red color) associated to PVDF and S associated to PESS (green color). In all cases, the bottom hydrophobic layer was deposited first (i.e., in contact with the aluminum foil). The top hydrophilic layer was deposited next (i.e., in contact with air). (For interpretation of the references to color in this figure legend, the reader is referred to the Web version of this article.)

hills and agglomerated clusters of nanofibers (See Fig. 2b). These structural features favor the formation of strongly adhered and compact composite nanofibrous structures. Conversely, the top layers of the DL-ENMs have nanofibrous structures with randomly distributed fibers and no bead formation (Fig. 2c). These results indicate that a post-treatment period of 0.5 h at 120 °C was sufficient to obtain ENMs with desirable properties, given the ability for electrospinning of the polymer solutions.

A marginal but consistent decrease in d_f of both hydrophobic and hydrophilic layers when considering different polymer types, such as PES, PES-OH, and PESS of DL-ENMs (Fig. 2d and e). This trend demonstrates a tendency in the order PES > PES-OH > PESS. However, based on the statistical calculations, these changes were insignificant. In general, the d_f*'s* of the hydrophilic layers are lower than those of the hydrophobic layers (PVDF) due to the lower viscosity of the PES, PES-OH, and PESS solution, (see Table 1). Under same parameters, high-viscosity polymer solutions result in higher d_f values, while high electrical conductivity results in low d_f values due to the stretching of electrospun fiber through the electrified jet along the gap between the needle tip and the metallic collector. It is evident that the viscosity has a dominant effect.

The morphology of ENMs are significantly influenced by the properties of the electrospinning polymer solutions, especially their viscosity and electrical conductivity [45]. Due to the stretching of the electrospun fiber in the electrified jet at the gap between the needle tip and the metal collector, less viscous polymer solutions will form membranes with lower d_f values if all other electrospinning parameters are maintained constant [46]. In addition, higher electrical conductivity favors the formation of thinner fibers by increasing the surface charge density of the solution jet and increasing its elongation under the influence of the applied electric field [45].

Furthermore, the d_f of the hydrophobic layer decreased when transitioning from the hydrophilic layers PVDF/PES, PVDF/PES-OH to PVDF/PESS (see Fig. 2b). And the reduction rate was 14.3%, 17.1%, and 25.7%, respectively, in comparison to the SL-ENM PVDF layer that was in contact with the aluminum foil (i.e., bottom layer), even though this hydrophobic layer was prepared from the same polymer solution (i.e., same viscosity). This reduction is mainly due to the compactness of the top hydrophilic layer, which slows down solvent evaporation from the bottom hydrophobic layer but also promotes the welding of the interlayers and nanofibers. However, such phenomena are less pronounced in DL-ENMs transitioning from PES to PESS with PES-OH as the top layer. This is mainly due to the looser structure formed in the top hydrophilic layer (i.e., from lower to higher electrical conductivity polymer solution), which leads to rapid evaporation of the solvent from the bottom layer, resulting in a fibrous structure with smaller fiber sizes.

Fig. 2e shows that when the hydrophilic layer was changed from PVDF/PES, PVDF/PES-OH to PVDF/PESS, the d_f of the hydrophilic layer decreased by 11.22%, 19.39%, and 26.53%, respectively, compared to the SL-ENM PVDF layer that was exposed to air (i.e., the top layer). In this regard, the PES polymer solution has the lowest electrical conductivity and the highest d_f among the hydrophilic layer, as shown in Table 1. On the contrary, the PESS polymer solution has the highest electrical conductivity and the lowest d_f, while the PES-OH polymer solution is in the middle in both aspects.

The EDS surface mapping of PESS DL-ENM (see Fig. 2f) shows a clear presence of PVDF-associated F (in red) in the hydrophobic layer and PESS-associated S (in green) in the hydrophilic layer.

Table 2 presents the total thickness (δ_t), water contact angle (θ_w), and mean fiber diameter (d_f) of each layer of the DL-ENMs and PVDF SL-ENMs. The corresponding void volume fractions (ε), mean interfiber spaces (d_i), and *LEP* values are also shown. It should be noted that the total electrospinning time for all prepared membranes was the same, which resulted in a δ_t of approximately 375 μm, considering the standard deviation of the measured values.

As shown in Table 2, the hydrophobic layer of the DL-ENMs has a water contact angle (θ_w) of more than 140.1°. The θ_w shows a sequential increase when changing the polymer from PESS to PES, and then to PES-OH in the following order (i.e., 140.1, 142.1, 143.1°, respectively). This is attributed to the nanofibrous network structure, the surface roughness, and the hydrophobicity nature of the base polymer (i.e., PVDF). Various studies have shown that surface roughness and morphology can strongly influence the hydrophobicity, and even dominate the effect of the material properties [47–50].

The DL-ENM void volume fraction (ε) also exhibited a dependence on the top layer, ascending in the sequence PES < PES-OH < PESS. This arrangement is in agreement with the relative openness observed in the SEM images of the top layer structures (see Fig. 2). The first deposited ENM (PVDF) bottom layer on the metallic collector impedes electrical charge dissipation toward the collector, acting as an electrical insulator and causing the formed fibers to repel each other, yielding an uncompacted fibrous network with a high ε. With an increase in electrical conductivity of the top deposited layer (see Table 1), the fibers of the bottom layer become finer, resulting in a looser and more open fibrous network. It is important to note that the ε values of the DL-ENM and SL-ENM are significantly higher than flat sheet membranes prepared by phase-inversion method (ranging between 26.8% and 79.6%) and commercial flat membranes commonly used in MD, such as Gelman's TF 200, TF 450, and TF 1000 polytetrafluoroethylene (PTFE) membranes

Table 2
Physical and structural properties of the prepared ENMs.

ENMs	δ_t (μm)	$(d_f)_{Bottom}$ (μm)	$(\theta_w)_{Bottom}$ (°)	$(d_f)_{Top}$ (μm)	$(\theta_w)_{Top}$ (°)	ε (%)	d_i (μm)	LEP_{H2O} (10^3 Pa)	$LEP_{35\ g/L}$ (10^3 Pa)
Before Gamma radiation									
PVDF	376.45 ±20.66	1.05 ±0.34	144.3 ±0.2	0.98 ±0.33	143.7 ±1.2	91.3 ±0.6	1.37 ± 0.03	64.50 ±0.71	68.00 ±1.41
PVDF-PES	368.61 ±17.13	0.90 ±0.37	143.1 ±0.1	0.87 ±0.32	122.5 ±0.8	93.2 ±0.4	1.67 ± 0.095	60.00 ±1.41	64.00 ±1.41
PVDF-PES-OH	373.55 ±33.81	0.87 ±0.22	142.1 ±0.1	0.79 ±0.12	113.2 ±1.4	94.5 ±0.3	1.99 ± 0.13	55.5 ±0.71	58.00 ±1.41
PVDF-PESS	379.29 ±15.29	0.79 ±0.26	140.3 ±0.2	0.72 ±0.22	103.5 ±2.1	96.1 ±0.4	2.15 ± 0.08	48.5 ±2.12	52.5 ±2.12

After Gamma radiation

ENMs	δ_t (μm)	ε (%)	LEP_{H2O} (10^3 Pa)	$LEP_{35\ g/L}$ (10^3 Pa)
PVDF	374.12 ± 18.33	84.2 ± 0.1	54.32 ± 0.66	57.20 ± 0.54
PVDF-PES	365.71 ± 12.33	87.4 ± 1.2	50.01 ± 1.32	52.34 ± 1.04
PVDF-PES-OH	372.66 ± 22.76	90.6 ± 0.8	49.54 ± 1.03	50.30 ± 1.23
PVDF-PESS	374.56 ± 34.21	92.3 ± 0.5	42.66 ± 1.56	46.43 ± 0.46

ENMs: electrospun nanofiber membranes; δ_t: total thickness; d_f: mean fiber diameter; θ_w: water contact angle of each layer; ε: void volume fraction; d_i: mean inter-fiber space; *LEP:* liquid entry pressure values obtained with distilled water and 35 g/L NaCl feed solutions.

with ε values between 64.3% and 68.7%, and Millipore's GVHP and HVHP PVDF membranes having ε values between 70.1 and 71.3% [51].

The mean inter-fiber space (d_i) of DL-ENMs depends on the top layer, as shown in Table 2. Specifically, it increases with increasing ε and decreasing top and bottom layer d_f. The open structure of the top layer and the variation of the d_f of the bottom layer can be attributed to this phenomenon. The PVDF-PESS ENM showed the highest d_i, which can be attributed to its low d_f and high ε. Conversely, the SL-ENMs exhibited smaller d_i than the DL-ENMs due to their compact structure and the low electrical conductivity of PVDF.

The *LEP* values of all ENMs were slightly higher in a 35 g/L NaCl aqueous solution compared to DI water (Table 2) due to the higher surface tension of the NaCl solution (76.87 ± 0.11 mN/m) compared with DI water (72.71 ± 0.09 mN/m) [52,53]. The *LEP* values of DL-ENMs vary with the identity of the top layer. This can be attributed to the change in the d_i. Notably, the trend in *LEP* values is consistent with the θ_w (see Table 2). The reported *LEP* values were comparable to those reported for other DL-ENMs [37,54].

The observed physical and structural properties of DL-ENM's indicate their suitability for MD application. This led us to investigate the effect of varying the support layer on desalination and decontamination by DCMD and AGMD.

3.2. MD performance

The first DCMD tests were carried out to investigate the effect of the feed temperature and the properties of the top layer on the DCMD performance. During the experiments, the hydrophobic layer (PVDF) of the DL-ENMs was positioned on the feed side of the DCMD system, whereas the hydrophilic layer was positioned on the permeate side.

ENMs with different supporting hydrophilic layers (PES, PES-OH, and PESS) were analyzed by DCMD at feed temperatures of 40–70 °C and NaCl concentrations of 0 and 35 g/L (see Fig. 3a). Fluxes were found to increase with feed temperature and were higher with distilled water (0 g/L NaCl) as feed compared to 35 g/L aqueous NaCl. This can be attributed to an Arrhenius-like dependence on feed temperature due to the increase in vapor pressure at the feed/ENM interface at higher temperatures. In addition, due to the concentration polarization effect and the decrease in water vapor pressure at the feed/ENM interface, increasing the salt concentration in the feed solution resulted in a decrease in permeate flux. DL-ENMs showed higher permeate flux than SL-ENMs, with the PVDF PESS membrane achieving the highest flux. This is attributed to the d_i and ε of the DL-ENMs as well as their respective hydrophilic supporting layers. Moreover, distilled water may penetrate easily into the inter-fiber space as a result of the more opened structure of the hydrophilic layers of the DL-ENMs and their propensity for wetting compared to the PVDF layer, resulting in a shorter liquid/vapor interface distance formed on both sides of the DL-ENMs [41,54].

The NaCl rejection factors observed for both DL-ENMs and PVDF SL-ENMs surpassed 99.96%, as shown in Fig. 3b. This remarkable performance can be attributed to their advantageous *LEP* values and small d_i, as presented in Table 1.

3.3. Desalination and SNWW treatment by MD before gamma-irradiation

Fig. 4 shows the permeate flux (J_p) values, electrical conductivity, and salt separation factor obtained for distilled feed water, aqueous salt solutions (35 g/L NaCl and 35 g/L $NaNO_3$), and aqueous salt solutions containing non-radioactive metal ions (450 ppm Cs^+, Cr^{3+} and Co^{2+} with 35 g/L $NaNO_3$) during MD experiments using the PVDF SL-ENM and the PVDF-PES, PVDF-PES-OH, and PVDF-PESS DL-ENMs. The salt separation factor and electrical conductivities of the resulting permeate are also shown in Fig. 4.

As shown in Fig. 4a, the PVDF SL-ENM exhibited a lower J_p value compared to all DL-ENMs. This is due to the fact that unlike the other DL-ENMs, which have more open structures and hydrophilic top layers with higher wetting propensities, PVDF SL-ENM has a lower ε of 91.3%. Consequently, DL-ENMs have shorter liquid-vapor interface distances on both sides of the membrane, resulting in higher permeate fluxes.

The PVDF-PESS DL-ENM showed the highest permeate fluxes, reaching values of 72.72 kg/m^{2}·h and 73.27 kg/m^{2}·h in the DCMD using aqueous feed solutions of NaCl and $NaNO_3$, respectively, in the DCMD. Additionally, it achieved 70.80 kg/m^{2}·h and 41.96 kg/m^{2}·h using aqueous feed solutions of SNWW in DCMD and AGMD, respectively. It is noteworthy that the permeate fluxes obtained for salt solutions and SNWW during MD experiments were slightly lower than those obtained using distilled water as feed. Because the water vapor pressure of the salt solution is inherently lower than that of the distilled water.

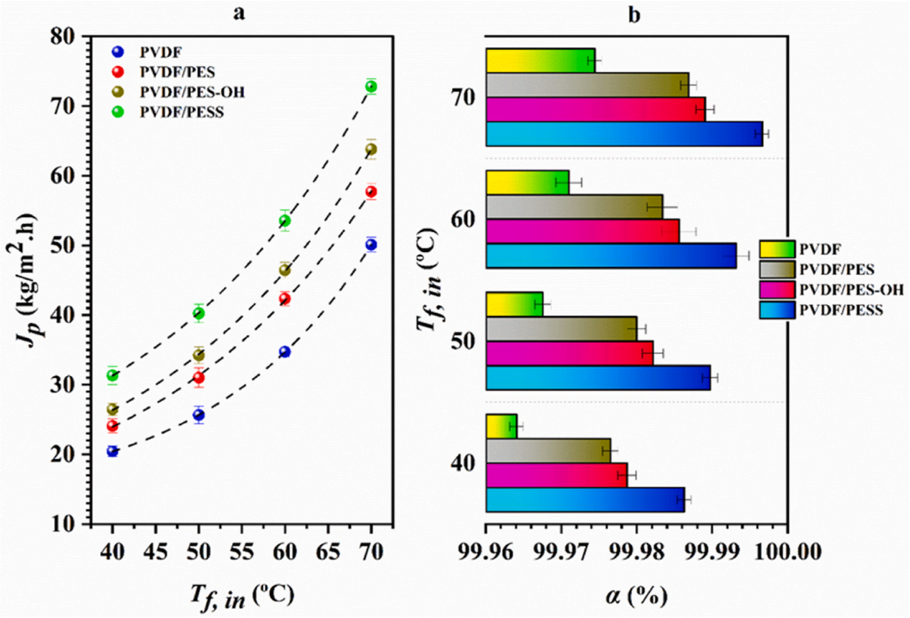

Fig. 3. a) Permeate flux values (J_p) and b) salt (NaCl) separation factors for the PVDF SL-ENM and the three DL-ENMs at different feed temperatures ($T_{f,in}$) when using a feed solution of 35 g/L aqueous NaCl. The curves plotted in the top figure show fits of the measured flux values to Arrhenius-type rate laws. The permeate temperature ($T_{p,in}$) was 20 °C, and the circulation flow rates of the feed and permeate liquid solutions were 1.25 L m^{-1} and 0.75 L m^{-1}, respectively.

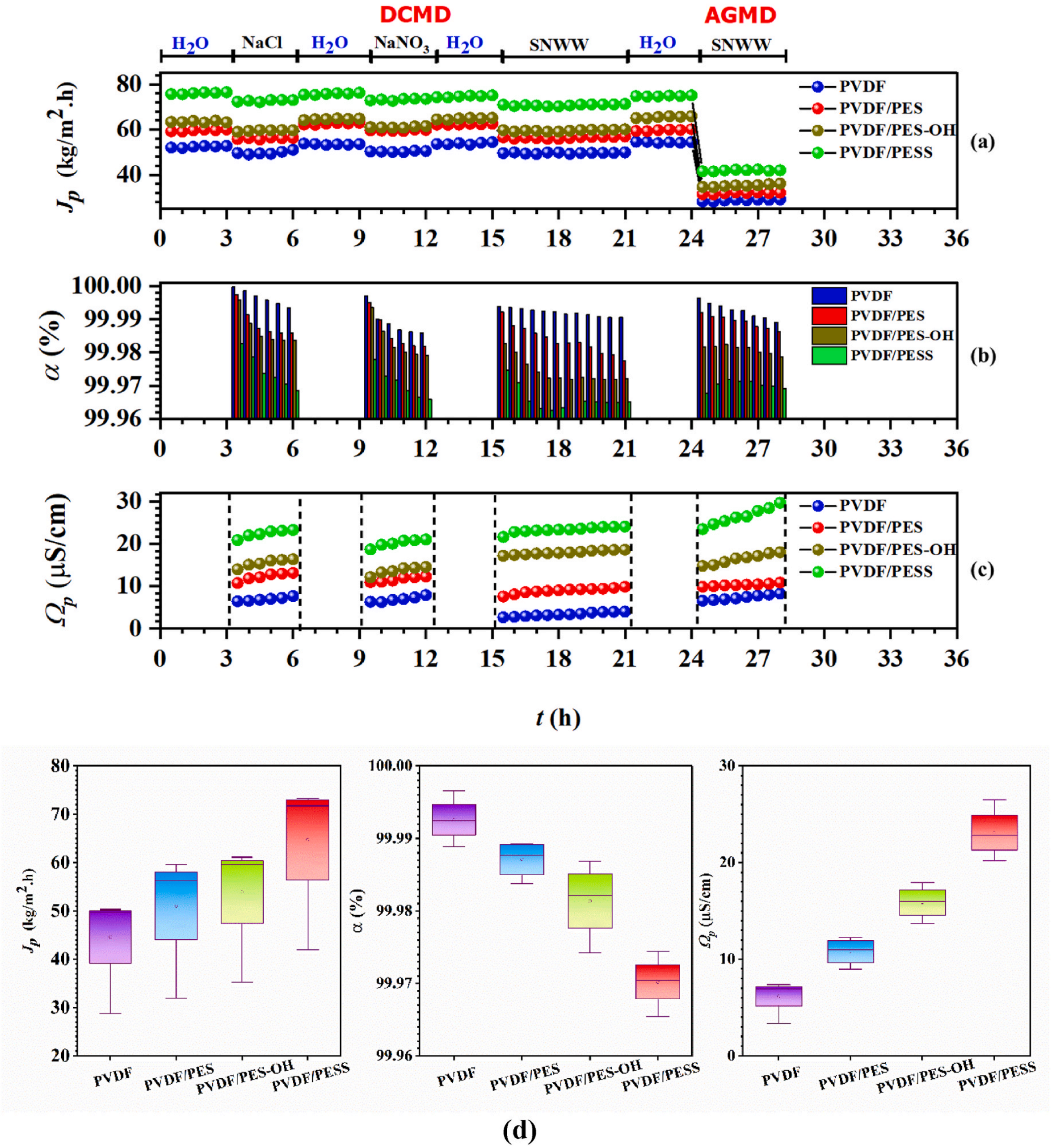

Fig. 4. Results from MD experiments using the PVDF SL-ENM and the three DL-ENMs before gamma irradiation with aqueous salt solutions and simulated nuclear wastewater (SNWW) as the feed solutions. The three stacked figures show a) the variation in the permeate flux over time, b) the variation in salt separation factors over time, c) the variation in the conductivity of the permeate over time, and d) the average salt separation factors achieved during the MD experiments for each membrane type and feed solution (H_2O, NaCl, $NaNO_3$, and SNWW).

In a nutshell, due to their more open structures and hydrophilic top layers, the DL-ENMs have shown superior performance in terms of permeate fluxes compared to the SL-ENMs because of their more open structures and hydrophilic top layers. Among the DL-ENMs, DL-ENMs with top PESS layer stand as a promising candidate for MD applications, showing the highest permeate flux.

The tested SL-ENMs and DL-ENMs consistently exhibited high salt rejections above 99.95% regardless of MD configuration and salt type (see Fig. 4b–d). Not only did the PVDF/PESS DL-ENM achieve the highest permeate fluxes, but it also produced permeate solutions with the highest ionic conductivities. However, the permeate ionic conductivity for both MD configurations remained below 30 μS/cm throughout the operating time, as shown in Fig. 4c. Compared to the PVDF SL-ENM and the other two DL-ENMs, these results were attributed to the large inter-fiber size of the d_i of the PVDF-PESS DL-ENM and the low value of the *LEP*.

In summary, with the PVDF/PESS DL-ENM exhibiting the highest permeate fluxes and electrical conductivities below 30 μS/cm, the tested ENMs demonstrated remarkable salt rejection capabilities. The suitability of these ENMs for desalination applications is suggested by the low permeate electrical conductivity observed in all configurations.

Fig. 5 shows the decontamination and metal ion rejection factors (expressed as percentages) for the PVDF SL-ENM and the PVDF/PES, PVDF/PES-OH, and PVDF/PESS DL-ENMs during MD of SNWW. Independent of the MD configuration, the degree of decontamination in the permeate decreased in the following order: SL-ENM PVDF > DL-ENM PVDF/PES > DL-ENM PVDF/PES-OH > DL-ENM PVDF/PESS. This outcome is consistent with the previously discussed variation in the void

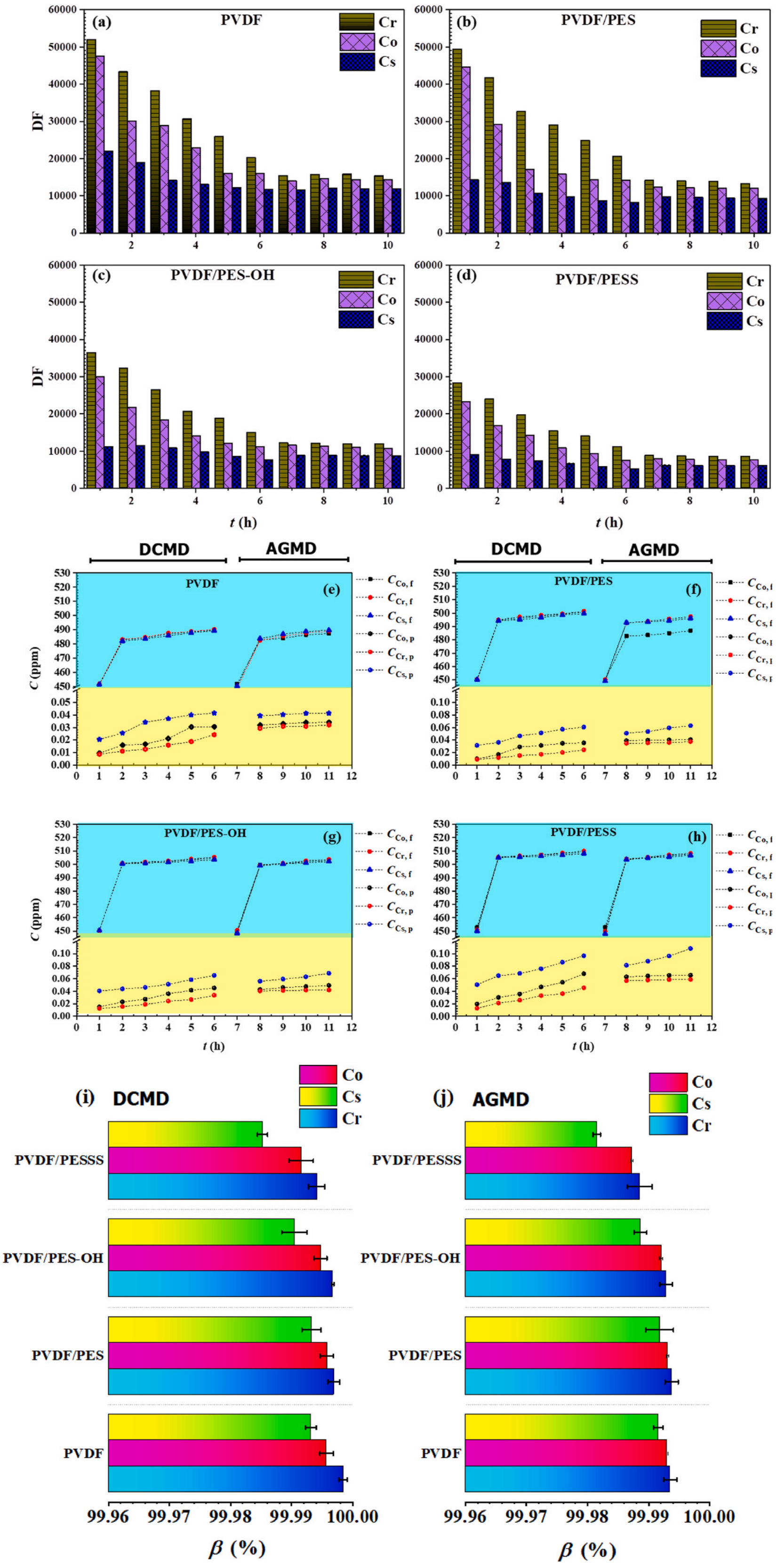

Fig. 5. DCMD and AGMD performance of PVDF membranes expressed in terms of the decontamination factor, DF (a: PVDF, b: PVDF/PES, c: PVDF/PES-OH, d: PVDF/PESS), and the measured metal ion concentration in the permeate and aqueous feed solution (e: PVDF, f: PVDF/PES, g: PVDF/PES-OH, h: PVDF/PESS). The decontamination factors achieved with each membrane (β, expressed in %) during DCMD (i) and AGMD (j) are also shown.

volume fractions of the ENMs (section 3.1 and Table 2).

The highest permeate fluxes for the treatment of SNWW by DCMD (70.80 kg/m^2·h) and AGMD (41.96 kg/m^2·h) were achieved using the PVDF/PESS DL-ENM (Fig. 4a). In the DCMD experiments, the metal ion content was reduced from around 450 ppm in the feed solution to 0.074 ppm in the permeate for Cs^+, 0.030 ppm for Cr^{3+}, and 0.042 ppm for Co^{2+}, corresponding to decontamination factors of 6996, 18799, and 13679, respectively. In the AGMD experiments using this membrane, the metal ion concentrations were reduced to 0.093 ppm for Cs^+, 0.058 ppm for Cr^{3+}, and 0.065 ppm for Co^{2+}, corresponding to decontamination factors of 5465, 8733, and 7836, respectively (Fig. 5c and h).

In 10-h operation (6 h for DCMD and 4 h for AGMD), the metal ion elimination efficiencies achieved with both MD configurations were above 99.98% (Fig. 5i and j). This suggests that MD can efficiently remove radionuclides from saline nuclear wastewater using ENMs, especially if a hydrophobic PVDF with a supporting hydrophilic PESS

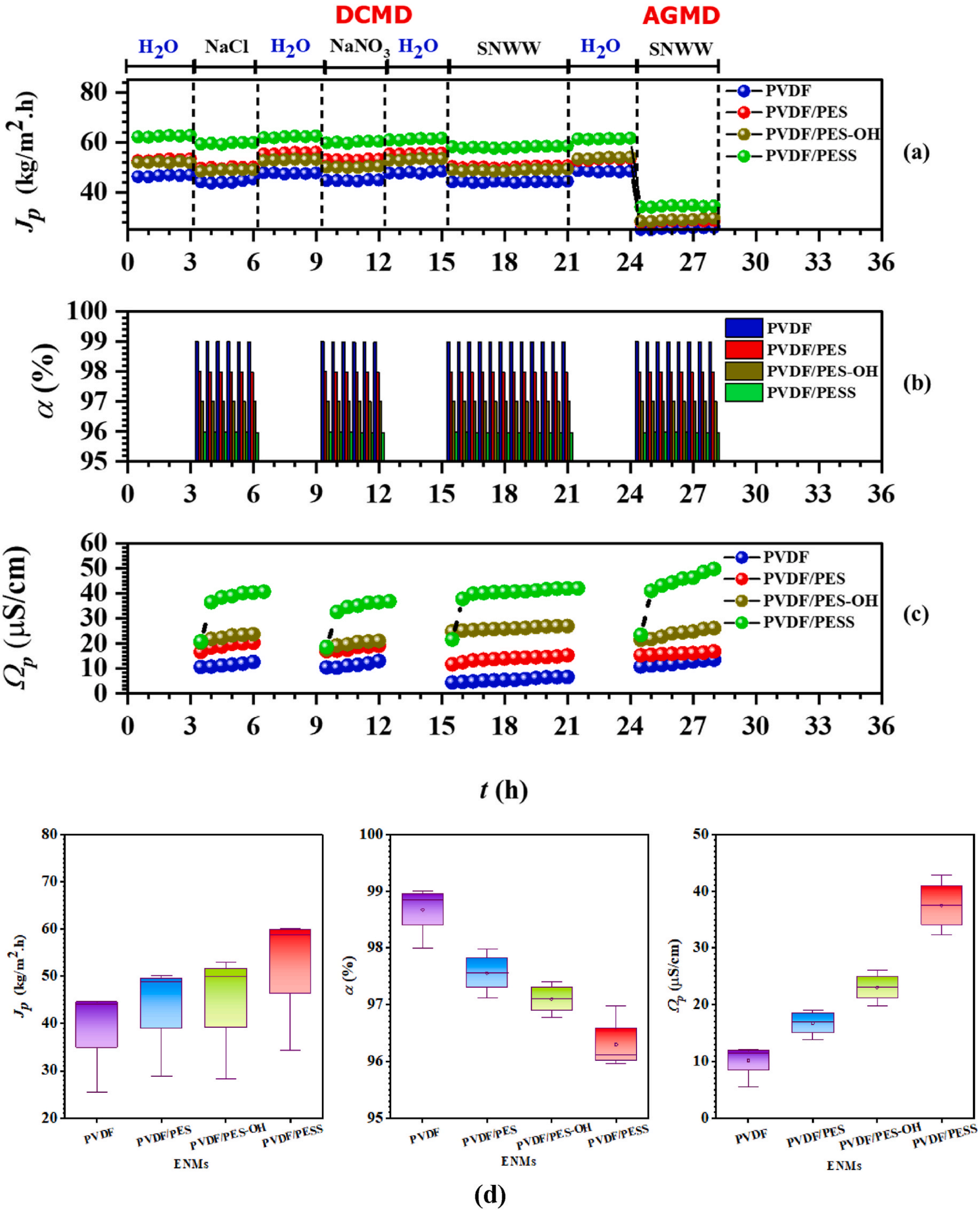

Fig. 6. Results from MD experiments using the PVDF SL-ENM and the three DL-ENMs after gamma irradiation with aqueous salt solutions and simulated nuclear wastewater (SNWW) as the feed solutions. The three stacked figures show a) the variation in the permeate flux over time, b) the variation in salt separation factors over time, c) the variation in the conductivity of the permeate over time, and d) the 3D-figure of the average salt separation factors achieved during the MD experiments for each membrane type and feed solution.

layer is used.

The permeate flux through the ENMs was re-measured using DI water as the feed solution after each experiment to detect any potential performance deterioration. It is evident from Fig. 4a, that no significant reduction in permeate flux was observed for any ENM, clearly demonstrating the robustness and integrity of prepared ENMs.

3.4. Desalination and SNWW treatment by MD after gamma-irradiation

Fig. 6 shows the values of the permeate flux (J_p) obtained for ENMs after gamma irradiation using DI feed water, aqueous salt solutions (35 g/L NaCl and 35 g/L $NaNO_3$), and SNWW aqueous solutions.

The PVDF-SL-ENM had a lower J_p value compared to both gamma-irradiated DL-ENMs and the unirradiated PVDF-SL-ENM (see Fig. 6a). This was due to its lower void volume fraction (84.2%) than the other DL-ENMs, which have higher porosities (ranging from 87.4% to 92.3%). In general, the J_p was slightly lower when the DL-ENMs were exposed to gamma radiation.

The salt rejection factors of the ENMs were lower than DL-ENMs without gamma irradiation and the permeate ionic conductivity was increased regardless of the MD configuration and the type of salt (see Fig. 6b and c). However, it is worth noting that the decontamination levels followed a similar trend to that of unirradiated ENM, as shown in Fig. 6c.

Gamma-irradiated ENMs metal ion removal efficiency was 97.98%, which is lower than the ENMs before irradiation (99.98%). Considering the exposure dosage and time this reduction in performance could be a determining factor in using PVDF as a hydrophobic layer in real-life decontamination of nuclear wastewater by MD. performance.

Fig. 7 shows the decontamination and rejection factors for ENMs after being subjected to gamma irradiation during the MD of the SNWW. The degree of decontamination in the permeate decreased in the following order, regardless of the MD configuration: SL-ENM > DL-ENM PVDF/PES > DL-ENM PVDF/PES-OH > DL-ENM PVDF/PESS, similar to the unirradiated ENMs. These results agree with the variation in the void volume fraction of the ENMs discussed earlier (see Table 2). The metal ion content in the permeate increased to relatively high values compared to unirradiated ENMs in both DCMD and AGMD experiments (see Fig. 7c–h). This result is consistent with the reduced *LEP* resulting from gamma irradiating ENMs (see Table 2).

The metal ion removal efficiencies achieved with both MD configurations were greater than 97.98% over 10 h of operation (6 h for DCMD and 4 h for AGMD) (Fig. 7i and j). This suggests that removing metal ions from SNWW by MD using ENMs and subjected to gamma irradiation may be less efficient compared to unirradiated ENMs, mainly due to the reduction of the *LEP* by increasing its tendency to wettability.

To evaluate the stability and degree of fouling of both irradiated and unirradiated ENMs after MD experiments, X-ray was used to investigate the presence of Co, Cr, and Cs on the surface of the ENM samples. Furthermore, the atomic percentages of Cr, Co, Cs, F, and carbon C, and the ratio of atomic percentages of each element to the sum of F + C for each ENM were measured by EDX (see Fig. 8 and Table S1). It is evident that with changing hydrophilic layer type, whether gamma-irradiated or not, the atomic percentages of each element (i.e., Co, Cr, and Cs) and their ratio (element/F + C) decrease. This is consistent with the DF levels recorded during MD testing, which was in the following sequence PVDF > PVDF/PES > PVDF/PES-OH > PVDF/PESS, shown in Figs. 5 and 7.

To gain a better understanding of the performance of the prepared membranes compared to previous studies and commercial Nanofiltration (NF) membranes, additional filtration experiments were conducted. The results are presented in Table 3. The prepared membranes in this study have a significantly higher permeate flux compared to the previously reported value for the decontamination of SNWW by MD, while maintaining the same level of rejection (>99.9%). In comparison with commercial NF membranes, the prepared membranes have a lower flux but a significantly higher rejection.

3.5. The effect of gamma-radiation

The chemical elements and functional groups present on the surfaces of both irradiated and unirradiated ENMs were characterized by FTIR and XPS analyses. In radioactive wastewater membrane processes, the irradiation effect on potential chemical changes in the membranes is often overlooked in practical applications. Therefore, this section focuses explicitly on the gamma radiation-induced alterations in ENMs. Our aim is to uncover the potential effects and transformations that occur at the molecular level, which can significantly impact the performance and stability of PVDF membranes used in the treatment of radioactive wastewater.

The FTIR result (Fig. 9a and b) shows that the deformation and stretching of $–CF_2$, and the $–CH_2$ at 875 cm^{-1}, 1068 cm^{-1}, and 1396 cm^{-1}, respectively; these peaks were identified as main characteristic features of PVDF, irrespective of whether the ENMs underwent irradiation or not. Upon irradiation, significant changes in the chemical structure of the ENMs were observed. A distinct new characteristic peak emerged in the irradiated ENMs between 1660 cm^{-1} and 1680 cm^{-1}, indicating alterations in the molecular bonds. This newly observed peak could be attributed to the stretching vibration of double bonds ($C{=}C$ or $C{=}O$). These observations strongly suggest that irradiation caused changes in the PVDF polymer structure leading to carbonyl groups forming in the chains. Moreover, this band can be generated by radical polymerization or the Michael addition reaction during the irradiation process [60–63].

For a rigorous analysis of the surface elemental composition of the irradiated and unirradiated ENMs, X-ray photoelectron spectroscopy (XPS) analysis was used. The characteristic XPS spectra of both irradiated and unirradiated ENMs are shown in Fig. 9c. The spectra showed characteristic peaks at 286 eV and 687.8 eV, respectively, corresponding to carbon (C-1s) and fluorine (F-1s) atoms associated with PVDF. In addition, at 532.08 eV, the characteristic peak of oxygen atoms (O-1s) was detected. Their atomic percentages were calculated for further analysis based on the peak intensities of these elements. The XPS analysis of the unirradiated ENMs did not detect any oxygen atoms on the surface.

Interestingly, the XPS spectra of the irradiated ENMs revealed the emergence of a new peak, indicating the presence of oxygen atoms on the surface of the irradiated ENMs. Conversely, the fluorine concentration (F-1s) and the fluorine/carbon (F-1s/C-1s) ratio exhibited a gradual decrease of 5.4% and 10.6%, respectively, as a consequence of irradiation. FTIR and XPS spectroscopy results confirmed the involvement of oxygen in reconstructing the surface structure of ENMs under irradiated conditions. Previous studies showed that PVDF is sensitive to irradiation, resulting in free radicals forming on the carbon backbone, particularly within the CF_2 and CH_2 groups [64–67]. The presence of molecular oxygen during the gamma irradiation process will accelerate the degradation of PVDF. The formed C-centered radicals react rapidly with molecular oxygen and lead to the formation of unstable peroxyl radicals [61,62,68]. The subsequently formed peroxides adversely affect the structural integrity of the PVDF fibers that make up ENMs. Consequently, the selectivity porosity, and properties of ENMs, which depend primarily on the inherent properties of the PVDF structure for their determination, are significantly affected by the degradation and destruction of the PVDF fiber structure. An incentive to reduce the hydrophobicity of ENMs would be the generation of new oxygen-containing functional groups. Therefore, the reduction of *LEP* values of irradiated ENMs (see Table 1) decreased the salts separation and decontamination factors of the nuclides during MD experiments.

In summary, radiation-induced changes can significantly affect the performance of ENMs during salt desalination and SNWW decontamination since the PVDF structure is the primary determinant of the permeability and efficiency of ENMs.

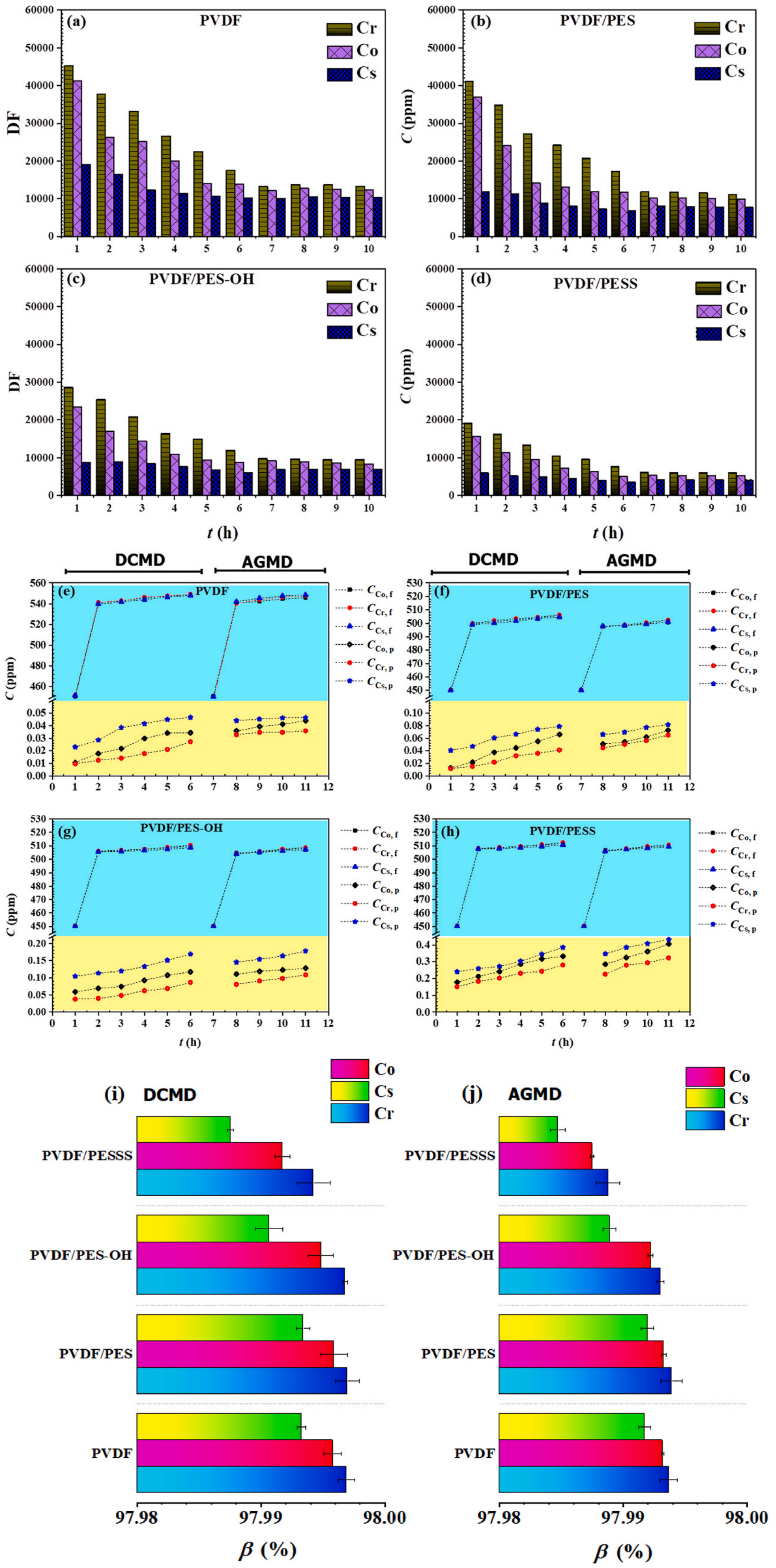

Fig. 7. DCMD and AGMD performance of membranes in terms of the decontamination factor, DF (a: PVDF, b: PVDF/PES, c: PVDF/PES-OH, d: PVDF/PESS), and the measured concentration of metal ions in the permeate and aqueous feed solution (e: PVDF, f: PVDF/PES, g: PVDF/PES-OH, h: PVDF/PESS). Furthermore, the rejection factors (β, expressed in %) achieved with each membrane in DCMD (i) and AGMD (j) are presented.

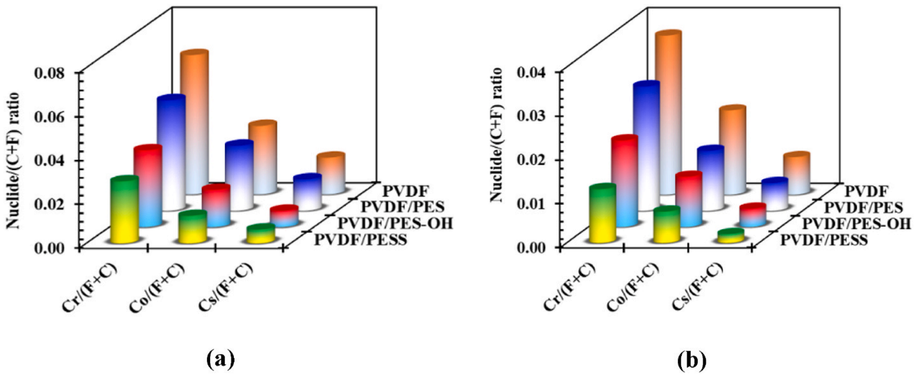

Fig. 8. Atomic composition of unirradiated and irradiated ENMs (F, C, Cr, Co, and Cs) by EDX analysis.

Table 3
Performance of previously reported membranes in SNWW treatment.

Filtration type	Membrane name	Condition	Flux (L·m^{-2} h^{-1})	α (%)	Ref
Nanofiltration	**ESNA1LF** **M_W: 200–300 Da**	Cr (III) at 450 ppm Co (II) at 450 ppm Cs (II) at 450 ppm $NaNO_3$ at 35 g/L P = 9 bar T = 22 °C	4.66	76.6 65.7 52.1 88,4	This study
	NANO-SW **M_W: 300 Da**		18.54	74.2 71.3 42.3 81.5	
	TriSep™ TS40 **M_W: 200Da**		17.32	83.4 79.4 66.2 91.3	
	TriSep™ TS80 **M_W: 150 Da**		15.65	87.1 89.4 79.1 93.2	
	Microdyn NP010 **M_W: 500 Da**		63.54	47.2 34.2 11.6 21.3	
	Microdyn NP030 **M_W: 1000 Da**		13.76	33.2 24.6 7.3 13.4	
	AFC 40	Co (II) at 100 ppm P = 25 bar pH = 3	250	97	[55]
	MWCNTs–interlinked GO	Sr (II) at 0.047 mmol/L pH = 10 P = 0.4 MPa	210.7	93.4	[56]
	TiO_2–doped ZrO_2	Co (II) at 1 ppm Sr (II) at 13 ppm Cs (II) at 7 ppm 0.2–0.8 MPa	35~40 L/(m^2·h·bar)	99.6 99.2 75.5	[57]
VMD	**PP**	Sr (II) at 10 ppm Co (II) at 11 ppm T_f: 70 °C T_p: 20 °C	6.71 6.30	99.60–99.74 99.67–99.82	[10]
VMD	**PTFE**	Cs(II) at 100 ppm Co(II) at 100 ppm Sr(II) at 100 ppm $NaNO_3$ at 80 g/L T_f: 75 P_v: 4 kPa	5.4	98.66 99.03 97.83	[58]
DCMD	**PVDF-NMP-CO_2-III**	Cr(III) at 450 ppm Co(II) at 450 ppm Cs(II) at 450 ppm	19.70	99.9804 99.9785 99.8548	[59]
DCMD	**PVDF-PESS DL-ENM**	$NaNO_3$ at 35 g/L T_f: 70 °C T_p: 20 °C	70.80	99.9941 99.9916 99.9852	This study
AGMD	**PVDF-PESS DL-ENM**		41.96	99.9885 99.9872 99.9815	

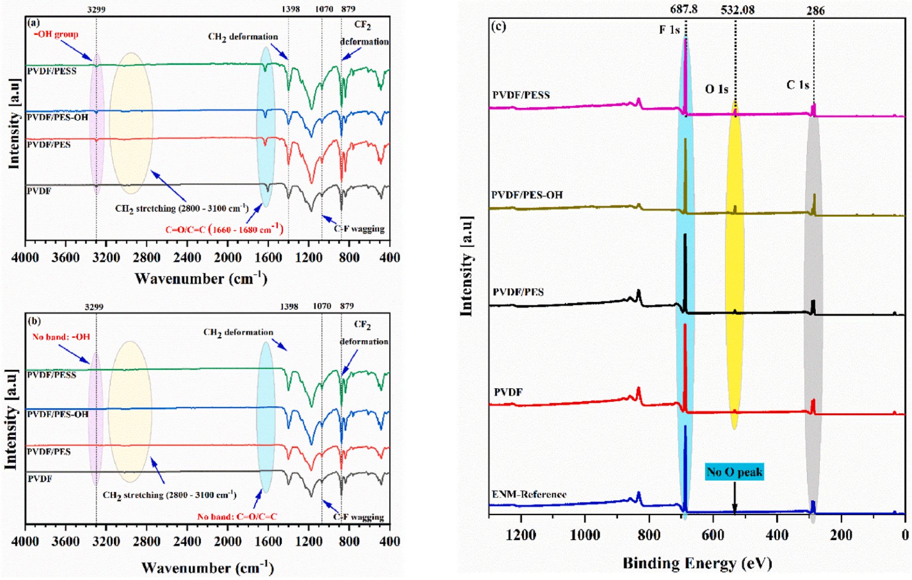

Fig. 9. FTIR spectra of irradiated (a) and unirradiated (b) ENMs, XPS spectra of irradiated ENMs, and unirradiated PVDF ENM (c).

4. Conclusion

This study demonstrates the efficacy of using electrospinning and combining two different polymers with different hydrophobicity to produce DL-ENM. These ENMs showed superior performance in desalination and radionuclide decontamination using DCMD and AGMD especially DL-ENMs.

In both DCMD and AGMD experiments, the DL-ENMs, especially the PVDF/PES, exhibited improved morphological and physical properties, resulting in significantly improved flux performance. Incorporating a PESS hydrophilic layer further enhanced the performance of the DL-ENM, achieving 1.49 to 1.47 times higher treatment efficiencies compared to SL-ENMs in various scenarios.

Despite achieving a low conductivity of 50 μS/cm and relatively high permeate fluxes for unirradiated ENMs, the influence of irradiation on the permeability and selectivity of irradiated ENMs was considerable. The separation factor of ENMs decreased by 2% upon exposure to Gamma radiation. The result of this study indicates that PVDF, a widely used fluoropolymer membrane in MD, is less suitable for long-term nuclear wastewater decontamination in real-life scenarios due to the instability of the polymer upon exposure to Gamma radiation. Nevertheless, this study demonstrated a better performance in terms of flux and rejection in comparison with the previously reported data and commercial membranes.

CRediT authorship contribution statement

Mohamed Essalhi: Writing – original draft, Investigation, Formal analysis, Data curation. **Noor Ul Afsar:** Writing – review & editing. **Denis Bouyer:** Writing – review & editing, Formal analysis, Conceptualization. **Ola Sundman:** Conceptualization, Resources, Writing – original draft. **Michael Holmboe:** Methodology, Validation, Writing – original draft. **Mohamed Khayet:** Writing – review & editing. **Mats Jonsson:** Data curation, Formal analysis, Methodology, Validation, Writing – original draft. **Naser Tavajohi:** Writing – review & editing, Conceptualization, Funding acquisition, Investigation, Project administration, Supervision.

Declaration of competing interest

The author declares that there is no conflict of interest.

Data availability

Data will be made available on request.

Acknowledgments

The authors would like to express their appreciation for the financial support provided by the Kempe Foundation (JCK22-0008). We also extend our gratitude to Professor Solomon Tesfalidet for his assistance with ICP measurements.

Appendix A. Supplementary data

Supplementary data to this article can be found online at https://doi.org/10.1016/j.memsci.2024.122726.

References

[1] P. Kumar, B. Kumar, D. Singh, Chapter 11—radioactive waste management, in: D. Yadav, P. Kumar, P. Singh, D.A. Vallero (Eds.), Hazardous Waste Management, 2022, pp. 289–301.
[2] A. Roychoudhury, S. Chakraborty, Chapter radioactive wastes: management by potential treatments, in: Waste Problems and Management in Developing Countries, first ed.s., Apple Academic Press, 2023, pp. 233–255.
[3] A. Al Faruque, Nuclear Energy Regulation, Risk and the Environment, first ed., Routledge, 2018.
[4] IAEA, Improvements of Radioactive Waste Management at WWER Nuclear Power Plants, IAEA Publications, Vienna, Austria, 2006. TECDOC-1492.
[5] G. Zakrzewska-Trznadel, M. Harasimowicz, A.G. Chmielewski, Membrane processes in nuclear technology-application for liquid radioactive waste treatment, Sep. Purif. Technol. 22 (2001) 617–625.
[6] S. Hashimoto, M. Komatsu, S. Miura, Radioactive materials released by the Fukushima nuclear accident, in: Forest Radioecology in Fukushima, Springer, Singapore, 2022, pp. 1–10.
[7] W. Lin, K. Yu, J. Du, H. Lin, W. Yu, M. Mo, Consequences of marine ecological environment and our preparedness for Fukushima radioactive wastewater discharge into the ocean, Chin. Sci. Bull. 66 (2021) 4500–4509.
[8] K.O. Buesseler, Opening the floodgates at Fukushima, Science 369 (2020) 621–622.
[9] M. Bergmann, F. Collard, J. Fabres, G.W. Gabrielsen, J.F. Provencher, C. M. Rochman, E. van Sebille, M.B. Tekman, Plastic pollution in the Arctic, Nat. Rev. Earth Environ. 3 (2022) 323–337.
[10] F. Jia, Y. Yin, J. Wang, Removal of cobalt ions from simulated radioactive wastewater by vacuum membrane distillation, Prog. Nucl. Energy 103 (2018) 20–27.
[11] F. Jia, J. Li, J. Wang, Y. Sun, Removal of strontium ions from simulated radioactive wastewater by vacuum membrane distillation, Ann. Nucl. Energy 103 (2017) 363–368.

[12] X. Wen, F. Li, X. Zhao, Removal of nuclides and boron from highly saline radioactive wastewater by direct contact membrane distillation, Desalination 394 (2016) 101–107.

[13] H. Liu, J. Wang, Separation of ammonia from radioactive wastewater by hydrophobic membrane contactor, Prog. Nucl. Energy 86 (2016) 97–102.

[14] M. Khayet, Treatment of radioactive wastewater solutions by direct contact membrane distillation using surface modified membranes, Desalination 321 (2013) 60–66.

[15] M. Khayet, J. Mengual, G. Zakrzewska-Trznadel, Direct contact membrane distillation for nuclear desalination, Part II: experiments with radioactive solutions, Int. J. Nucl. Desalination 2 (2006) 56–73.

[16] IAEA-TECDOC-1336, Combined Methods for Liquid Radioactive Waste Treatment. Final Report of a Co-ordinated Research Project 1997-2001, IAEA, 2003.

[17] G. Gedda, K. Balakrishnan, R.U. Devi, K.J. Shah, V. Gandhi, V. Gandh, K. Shah, Chapter 1—Introduction to conventional wastewater treatment technologies: limitations and recent advances, in: Adv. Wastewater Treat. I, 2021, p. 91.

[18] G. Crini, E. Lichtfouse, Wastewater Treatment: an Overview, Springer, Cham, 2018, pp. 1–21.

[19] H. Ma, M. Shen, Y. Tong, X. Wang, Radioactive wastewater treatment technologies: a review, Molecules 28 (2023) 1935.

[20] X. Zhang, P. Gu, Y. Liu, Decontamination of radioactive wastewater: state of the art and challenges forward, Chemosphere 215 (2019) 543–553.

[21] H. Liu, J. Wang, Treatment of radioactive wastewater using direct contact membrane distillation, J. Hazard Mater. 261 (2013) 307–315.

[22] S. Hube, M. Eskafi, K.F. Hrafnkelsdóttir, B. Bjarnadóttir, M.Á. Bjarnadóttir, S. Axelsdóttir, B. Wu, Direct membrane filtration for wastewater treatment and resource recovery: a review, Sci. Total Environ. 710 (2020) 136375.

[23] D. Rana, T. Matsuura, M.A. Kassim, A.F. Ismail, Radioactive decontamination of water by membrane processes — a review, Desalination 321 (2013) 77–92.

[24] J. Wang, S. Zhuang, Removal of cesium ions from aqueous solutions using various separation technologies, Rev. Environ. Sci. Biotechnol. 18 (2019) 231–269.

[25] X. Liu, J. Wu, J. Wang, Removal of Cs(I) from simulated radioactive wastewater by three forward osmosis membranes, J. Chem. Eng. 344 (2018) 353–362.

[26] A.K. Pabby, B. Swain, N.L. Sonar, V.K. Mittal, T.P. Valsala, S. Ramsubramanian, D. B. Sathe, R.B. Bhatt, S. Pradhan, Radioactive waste processing using membranes: state of the art technology, challenges and perspectives, Separ. Purif. Rev. 51 (2022) 143–173.

[27] A.A. Alsarayreh, T.K. Abbas, S.O. Alaswad, A.D. Bajoga, Remove liquid radioactive wastes utilizing nanofiltration, ultrafiltration, and microfiltration membranes, Eng. Technol. J. 40 (2022) 1231–1259.

[28] R. Li, H. Yan, H. Wang, J. Yan, C. Jiang, Y. Wang, T. Xu, Electrodialysis for the volume reduction of the simulated radionuclides containing seawater, J. Hazard Mater. 439 (2022) 129601.

[29] K.P. Lopez, R. Wang, E.A. Hjelvik, S. Lin, A.P. Straub, Toward a universal framework for evaluating transport resistances and driving forces in membrane-based desalination processes, Sci. Adv. 9 (2023) eade0413.

[30] M. Essalhi, M. Khayet, Fundamentals of Membrane Distillation, Woodhead Publishing, Oxford, 2015, pp. 277–316.

[31] A. Alkhudhiri, N. Darwish, N. Hilal, Membrane distillation: a comprehensive review, Desalination 287 (2012) 2–18.

[32] A.M. Alklaibi, N. Lior, Membrane-distillation desalination: status and potential, Desalination 171 (2005) 111–131.

[33] M.K. Purkait, R. Singh, Membrane Technology in Separation Science, CRC Press, 2018.

[34] L. Francis, F.E. Ahmed, N. Hilal, Electrospun membranes for membrane distillation: the state of play and recent advances, Desalination 526 (2022) 115511.

[35] J. Lee, C. Boo, W.-H. Ryu, A.D. Taylor, M. Elimelech, Development of omniphobic desalination membranes using a charged electrospun nanofiber scaffold, ACS Appl. Mater. Interfaces 8 (2016) 11154–11161.

[36] S.S. Ray, S.-S. Chen, C.-W. Li, N.C. Nguyen, H.T. Nguyen, A comprehensive review: electrospinning technique for fabrication and surface modification of membranes for water treatment application, RSC Adv. 6 (2016) 85495–85514.

[37] M. Khayet, M.C. García-Payo, L. García-Fernández, J. Contreras-Martínez, Dual-layered electrospun nanofibrous membranes for membrane distillation, Desalination 426 (2018) 174–184.

[38] S. Huang, J. Mansouri, P. Le-Clech, G. Leslie, C.Y. Tang, A.G. Fane, A comprehensive review of electrospray technique for membrane development: Current status, challenges, and opportunities, J. Membr. Sci. 646 (2022) 120248.

[39] J. Zuo, T.-S. Chung, G.S. O'Brien, W. Kosar, Hydrophobic/hydrophilic PVDF/Ultem® dual-layer hollow fiber membranes with enhanced mechanical properties for vacuum membrane distillation, J. Membr. Sci. 523 (2017) 103–110.

[40] M. Essalhi, M. Khayet, S. Tesfalidet, M. Alsultan, N. Tavajohi, Desalination by direct contact membrane distillation using mixed matrix electrospun nanofibrous membranes with carbon-based nanofillers: a strategic improvement, J. Chem. Eng. 426 (2021) 131316.

[41] L. Zhao, C. Wu, X. Lu, D. Ng, Y.B. Truong, J. Zhang, Z. Xie, Theoretical guidance for fabricating higher flux hydrophobic/hydrophilic dual-layer membranes for direct contact membrane distillation, J. Membr. Sci. 596 (2020) 117608.

[42] X. Jia, L. Lan, X. Zhang, T. Wang, Y. Wang, C. Ye, J. Lin, Pilot-scale vacuum membrane distillation for decontamination of simulated radioactive wastewater: system design and performance evaluation, Sep. Purif. Technol. 275 (2021) 119129.

[43] X. Wen, F. Li, B. Jiang, X. Zhang, X. Zhao, Effect of surfactants on the treatment of radioactive laundry wastewater by direct contact membrane distillation, J. Chem. Technol. Biotechnol. 93 (2018) 2252–2261.

[44] C.J. Davey, P. Liu, F. Kamranvand, L. Williams, Y. Jiang, A. Parker, S. Tyrrel, E. J. McAdam, Membrane distillation for concentrated blackwater: influence of configuration (air gap, direct contact, vacuum) on selectivity and water productivity, Sep. Purif. Technol. 263 (2021) 118390.

[45] C.J. Angammana, S.H. Jayaram, Analysis of the effects of solution conductivity on electrospinning process and fiber morphology, IEEE Trans. Ind. Appl. 47 (2011) 1109–1117.

[46] M.B. Abid, R.A. Wahab, M.A. Salam, I.A. Moujdin, L. Gzara, Desalination technologies, membrane distillation, and electrospinning, an overview, Heliyon 9 (2023) e12810.

[47] Q. Zheng, C. Lü, Size effects of surface roughness to Superhydrophobicity, Procedia IUTAM 10 (2014) 462–475.

[48] D. Quéré, Rough ideas on wetting, Physica A Stat. Mech. Appl. 313 (2002) 32–46.

[49] A. Raman, J.S. Jayan, B.D.S. Deeraj, A. Saritha, K. Joseph, Electrospun nanofibers as effective superhydrophobic surfaces: a brief review, Surface. Interfac. 24 (2021) 101140.

[50] H. Zhou, H. Wang, H. Niu, T. Lin, Electrospun fibrous membranes with super-large-strain electric superhydrophobicity, Sci. Rep. 5 (2015) 15863.

[51] M. Khayet, Membranes and theoretical modeling of membrane distillation: a review, Adv. Colloid Interface Sci. 164 (2011) 56–88.

[52] X. Wang, C. Chen, K. Binder, U. Kuhn, U. Pöschl, H. Su, Y. Cheng, Molecular dynamics simulation of the surface tension of aqueous sodium chloride: from dilute to highly supersaturated solutions and molten salt, Atmos. Chem. Phys. 18 (2018) 17077–17086.

[53] O. Ozdemir, S.I. Karakashev, A.V. Nguyen, J.D. Miller, Adsorption and surface tension analysis of concentrated alkali halide brine solutions, Miner. Eng. 22 (2009) 263–271.

[54] L.D. Tijing, Y.C. Woo, M.A.H. Johir, J.-S. Choi, H.K. Shon, A novel dual-layer bicomponent electrospun nanofibrous membrane for desalination by direct contact membrane distillation, J. Chem. Eng. 256 (2014) 155–159.

[55] C.-V. Gherasim, K. Hancková, J. Palarčík, P. Mikulášek, Investigation of cobalt(II) retention from aqueous solutions by a polyamide nanofiltration membrane, J. Membr. Sci. 490 (2015) 46–56.

[56] L. Zhang, Y. Lu, Y.L. Liu, M. Li, H.Y. Zhao, L.A. Hou, High flux MWCNTs-interlinked GO hybrid membranes survived in cross-flow filtration for the treatment of strontium-containing wastewater, J. Hazard Mater. 320 (2016) 187–193.

[57] Y. Lu, T. Chen, X. Chen, M. Qiu, Y. Fan, Fabrication of TiO_2-doped ZrO_2 nanofiltration membranes by using a modified colloidal sol-gel process and its application in simulative radioactive effluent, J. Membr. Sci. 514 (2016) 476–486.

[58] X. Wen, F. Li, X. Zhao, Filtering of low-level radioactive wastewater by means of vacuum membrane distillation, Nucl. Technol. 194 (2016) 379–386.

[59] M. Essalhi, N. Ismail, S. Tesfalidet, J. Pan, Q. Wang, Z. Cui, M.C. García-Payo, M. Khayet, J.-P. Mikkola, S. Sarmad, D. Bouyer, Y. Zhao, B. Li, C. André Ohlin, N. Tavajohi, Polyvinylidene fluoride membrane formation using carbon dioxide as a non-solvent additive for nuclear wastewater decontamination, J. Chem. Eng. 446 (2022) 137300.

[60] H. Wang, B. Yan, Z. Hussain, W. Wang, N. Chang, Chemically graft aminated GO onto dehydro-fluorinated PVDF for preparation of homogenous DF-PVDF/GO-NH_2 ultrafiltration membrane with high permeability and antifouling performance, Surface. Interfac. 33 (2022) 102255.

[61] Y. Guo, C. Liu, H. Liu, W. Wang, H. Li, C. Zhang, Influences of gamma-ray irradiation on PVDF membrane behavior: an experimental study based on simulation and numerical analysis, Polym. Degrad. Stabil. 193 (2021) 109722.

[62] J.S. Forsythe, D.J.T. Hill, The radiation chemistry of fluoropolymers, Prog. Polym. Sci. 25 (2000) 101–136.

[63] B.J. Lyons, Radiation crosslinking of fluoropolymers—a review, Radiat. Phys. Chem. 45 (1995) 159–174.

[64] S. Allayarov, L. Kalinin, D. Dixon, E. Tolstopyatov, I. Frolov, L. Ivanov, P. Grakovich, O. Golodkov, Comparative investigation by infrared spectroscopy of the conformational metamorphosis of polyvinylidene fluoride under the action of an infrared laser and of γ-irradiation, J. Russ. Laser Res. 40 (2019) 356–363.

[65] S.R. Allayarov, Y.A. Olkhov, D.A. Dixon, Effect of radiation from an infrared laser and γ-rays from ^{60}Co on the molecular–topological structure of polyvinylidene fluoride, J. Russ. Laser Res. 38 (2017) 482–489.

[66] M.M. Nasef, H. Saidi, K.Z.M. Dahlan, Investigation of electron irradiation induced-changes in poly(vinylidene fluoride) films, Polym. Degrad. Stabil. 75 (2002) 85–92.

[67] X. Huang, W. Wang, Y. Liu, H. Wang, Z. Zhang, W. Fan, L. Li, Treatment of oily waste water by PVP grafted PVDF ultrafiltration membranes, J. Chem. Eng. 273 (2015) 421–429.

[68] R. Jiménez-Robles, M. Izquierdo, V. Martínez-Soria, L. Martí, A. Monleón, J. D. Badia, Stability of superhydrophobicity and structure of PVDF membranes treated by vacuum oxygen plasma and organofluorosilanisation, Membranes 13 (2023) 314.